Long lifetime and selective accumulation of the A-type lamins accounts for the tissue specificity of Hutchinson-Gilford progeria syndrome

Authors: John Hasper[1], Kevin Welle[2], Kyle Swovick[2], Jennifer Hryhorenko[2], Sina Ghaemmaghami[2,3], Abigail Buchwalter[1,4,5]

Affiliations:

[1]Cardiovascular Research Institute, University of California, San Francisco, San Francisco, CA

[2]University of Rochester Mass Spectrometry Resource Laboratory, Rochester, NY

[3]Department of Biology, University of Rochester, Rochester, NY

[4]Department of Physiology, University of California, San Francisco, San Francisco, CA

[5]Chan Zuckerberg Biohub, San Francisco, CA

Abstract

Mutations to the *LMNA* gene cause laminopathies including Hutchinson-Gilford progeria syndrome (HGPS). The origins of tissue specificity in these diseases are unclear, as the A-type Lamins are abundant and broadly expressed proteins. We show that A-type Lamin protein and transcript levels are uncorrelated across tissues. As protein-transcript discordance can be caused by variations in protein lifetime, we applied quantitative proteomics to profile protein turnover rates in healthy and progeroid tissues. We discover that tissue context and disease mutation each influence A-type Lamin protein lifetime. Lamin A/C has a weeks-long lifetime in the aorta, heart, and fat, but a days-long lifetime in tissues spared from disease. Progerin is even more long-lived than Lamin A/C in the cardiovascular system and accumulates there over time. These proteins are insoluble and densely bundled in cardiovascular tissues, which may present an energetic barrier to degradation. We reveal that human disease alleles are significantly over-represented in the long-lived proteome. These findings indicate that gene therapy interventions will have significant latency and limited potency in disrupting long-lived disease-linked proteins such as Progerin.

Introduction

The nuclear lamina is an intermediate filament meshwork that underlies the nuclear envelope. In mammals, this structure is composed of two classes of Lamin proteins: the “A-type” lamins (Lamins A and C), and the “B-type” lamins (Lamins B1 and B2). Lamins assemble into bundled filaments that strengthen the nucleus and scaffold the genome.

The *LMNA* locus encodes the Lamin A and C proteins and is a hotspot for disease-linked mutations; hundreds of mutations to *LMNA* have been linked to at least 15 distinct syndromes, collectively referred to as “laminopathies”(*1*). While the Lamin A/C proteins are broadly expressed, laminopathies primarily afflict the cardiovascular system, muscle, bone, and fat(*1*). Hutchinson-Gilford progeria syndrome (HGPS) is a rare and devastating autosomal dominant laminopathy that resembles physiological aging at an accelerated rate, with rapid deterioration of the skin, adipose tissue, and cardiovascular system. Most cases of HGPS are caused by a single base pair substitution (GGC > GGT) that activates a cryptic splice site, resulting in the in-frame deletion of a portion of exon 11 in *LMNA* and the production of a toxic, dominant negative “Progerin” protein.

Several gene therapy approaches have recently been tested in mouse models of HGPS, ranging from disrupting the mutant allele with CRISPR/Cas9 indels(*2*, *3*), correcting the mutant allele with base editing(*4*), or interfering with the unique RNA splicing event that produces the *Progerin* transcript(*5*–*8*). Because HGPS is caused by the toxic effects of a dominant negative protein, an effective gene therapy will need to induce the removal and replacement of as much of the Progerin protein as possible. However, recent work indicates that gene therapies have variable effects on Progerin protein levels *in vivo*; for instance, in various treatment regimes that effectively clear the mutant protein from the liver, the protein persists to some extent in the cardiovascular system (*3*–*6*, *8*, *9*). In one particularly striking case, high levels of Progerin were found to persist in the cardiovascular system after over 5 months of treatment with splice-interfering antisense oligonucleotides, long after effective depletion of the *Progerin* transcript had been achieved (*6*). Altogether, these findings indicate that removing Progerin protein is a major bottleneck that may limit the potency of HGPS gene therapies.

Why is Progerin so intractable to removal in the cardiovascular system? Progerin could be produced in particularly high amounts in cardiovascular tissues, which are known to express high levels of Lamin A/C(*10*). A second, non-exclusive possibility is that Progerin is especially long-lived in the cardiovascular system. Notably, the closely related B-type Lamin proteins have extremely long lifetimes of months to years in the murine nervous system(*11*, *12*). The lifetimes

68 of the A-type Lamins within tissues have not been defined. We previously profiled protein lifetimes
69 in cultured progeroid fibroblasts and found no evidence that the HGPS-causative mutation impairs
70 the turnover of Lamin A/C(*13*). However, these experiments could not address the potential
71 influence of tissue context on the turnover rate of Lamin A/C and/or Progerin.
72 Here, we deploy our recently developed dynamic proteomic approach, turnover and
73 replication analysis by isotope labeling (TRAIL)(*14*) to define the turnover rate of the Lamin A/C
74 and Progerin proteins within tissues of healthy and progeroid mice. We report that Lamin A/C
75 turns over an order of magnitude more slowly within disease-afflicted tissues compared to
76 disease-spared tissues. Further, we show that the Progerin mutant is even more long-lived than
77 wild-type Lamin A/C in the cardiovascular system, leading us to estimate a months-long lifetime
78 of this toxic mutant protein in these diseased tissues. In contrast, we show that protein abundance
79 does not correlate with disease susceptibility in human or mouse tissues. By evaluating the
80 incidence of human disease alleles across protein turnover deciles, we reveal that human disease
81 alleles are generally over-represented in the long-lived proteome. These findings have major
82 implications for both the pathogenesis and treatment of laminopathies and establish a novel
83 paradigm for rare human diseases caused by the action of long-lived mutant proteins.
84
85 **Results**
86
87 ***High abundance of Lamin A/C/Progerin proteins is not restricted to cardiovascular tissues***
88
89 High Progerin abundance could both drive disease and thwart gene therapies. We
90 reasoned that tissues that express high levels of Lamin A/C in healthy individuals may also
91 express more Progerin in diseased individuals, and we mined a quantitative proteomic atlas of 29
92 human tissues(*15*) to systematically evaluate the relationship between Lamin A/C protein
93 expression and laminopathy pathology. This tissue proteome atlas relies on intensity-based
94 absolute quantification (iBAQ) to accurately quantify protein abundance(*16*) and on the histone-
95 based "proteomic ruler" approach(*17*) to estimate protein copy numbers per cell. These data
96 indicate that the human Lamin A/C proteins are extremely abundant in smooth muscle (Fig. 1A),
97 consistent with previous reports in mouse tissues(*18*, *19*). Because vascular smooth muscle is
98 prominently affected in *LMNA*-linked Hutchinson-Gilford progeria syndrome(*20*, *21*), these data
99 could suggest that high Lamin A/C abundance correlates with disease vulnerability. However, the
100 heart and adipose tissue are also afflicted in HGPS and other laminopathies, but these tissues
101 express Lamin A/C at a level comparable to many unaffected human tissues (Fig. 1A). In fact,

102 26/29 of the analyzed tissues are estimated to produce more than 10^7 copies of Lamin A/C per
103 cell (Fig. S1A), indicating that high expression levels of Lamin A/C are not sufficient to drive
104 disease.

105 The abundance ratio of the A-type (Lamin A/C) to B-type (Lamin B1 and B2) lamins
106 influences nuclear mechanics(*18*) and it has been proposed that tissues with a high ratio of A-
107 type:B-type lamins might be most sensitive to *LMNA* mutations(*19*). Consistent with previous
108 analyses in the mouse(*19*), the ratio of A-type:B-type lamins is very high in the human heart
109 (8.6:1), smooth muscle (7.2:1), and fat (4.3:1) which are especially vulnerable to *LMNA* mutations
110 (Fig. S1D). However, this ratio is also comparably high in many unaffected tissues (Fig. S1D).
111 Therefore, a high ratio of A-type to B-type Lamins is not sufficient to drive HGPS.

112 We next considered the alternative possibility that Progerin abundance varies
113 independently of Lamin A/C abundance across diseased tissues. The genetic lesion that causes
114 HGPS activates a cryptic splice site, resulting in the in-frame deletion of a portion of exon 11 in
115 *LMNA* without altering the shorter *LMNC* isoform (Fig. 1B). This splice site operates with
116 incomplete efficiency, such that both *Progerin* and wild type *LMNA* transcripts can be produced
117 from the mutant allele; variable splice site use could thus modulate *Progerin* production across
118 tissues(*22*). To explore this possibility, we turned to a genetically modified mouse model that
119 harbors the HGPS-causative C>T substitution in the endogenous mouse *LMNA* locus
120 ($LMNA^{G609G/+}$)(*5*).

121 We evaluated the proportional abundance of the Lamin A, Lamin C, and Progerin proteins
122 by Western blotting across tissues in wild type (Fig. S2) and progeroid mice (Fig. 1C-D) by
123 detection with an antibody that detects an epitope shared across all A-type lamins (see Methods).
124 We reasoned that this approach was the most relevant way to quantify the dose of the toxic
125 Progerin protein, as the ratio of Progerin to other wild type Lamin isoforms has been proposed to
126 influence pathology(*19*). We found that Progerin contributes significantly to the total amount of A-
127 type Lamins detected in many tissues - up to 50% in some cases(Fig. 1C-D). Puzzlingly, however,
128 the proportional abundance of Progerin does not correlate with HGPS pathology; the disease
129 variant is highly abundant in afflicted tissues, such as the aorta and adipose tissue, as well as in
130 tissues that remain functional, such as the kidney and large intestine. Altogether, these analyses
131 indicate that protein abundance alone cannot explain either the vulnerability of specific tissues to
132 *LMNA* mutations or the resistance of Progerin to therapeutic interventions.

Figure 1.

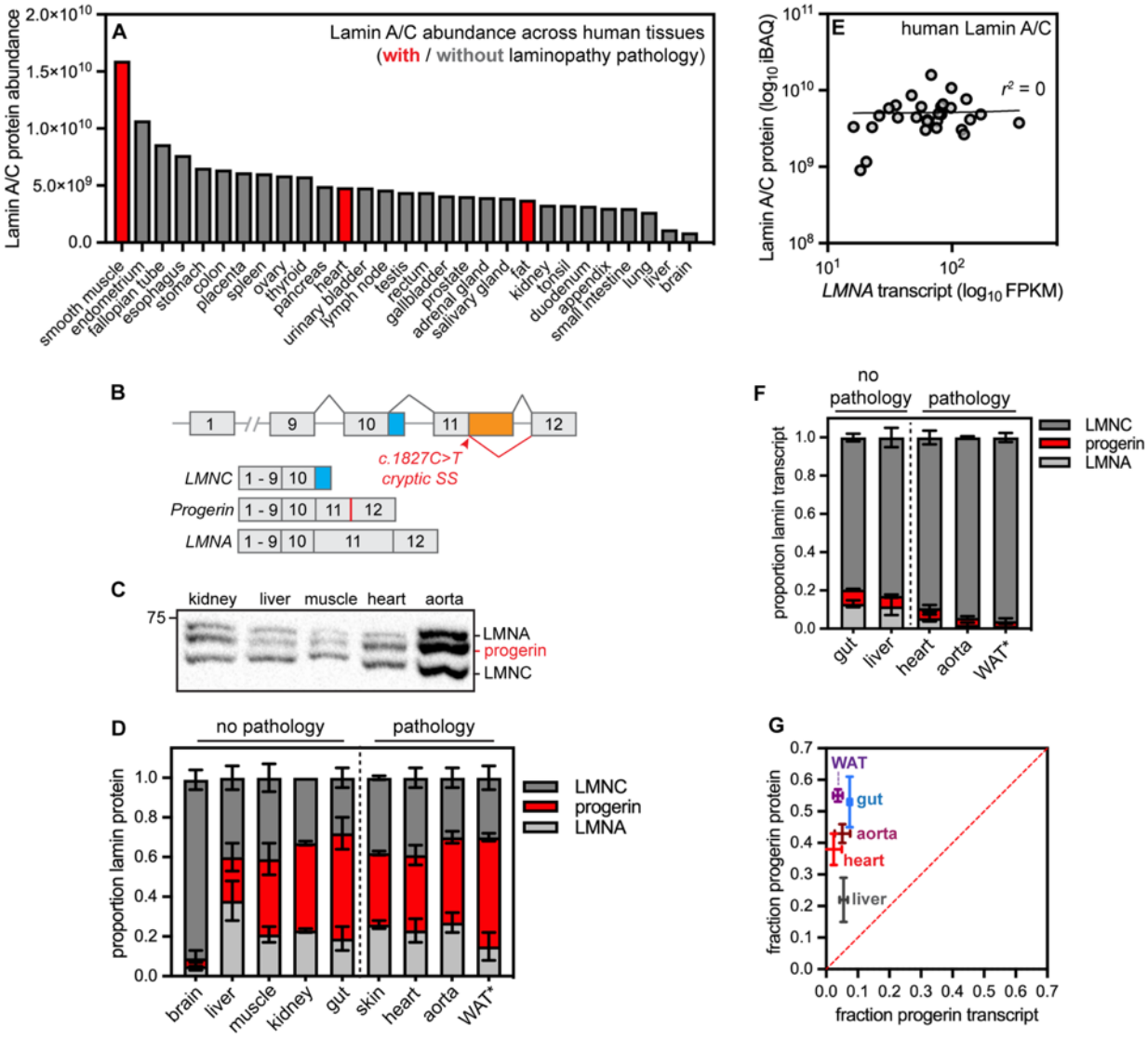

Figure 1. Poor correlation between trasncript and protein abundance for the long-lived disease-linked protein Lamin A/C. (A) iBAQ quantification of Lamin A/C absolute protein abundance across 29 human tissues. Data reanalyzed from Wang et al., *Mol Syst Biol* 2019. (B) Diagram of the *LMNA* locus, which produces the *LMNA* (exons 1-12) and *LMNC* (exons 1-10) transcripts. In HGPS, a base pair substitution activates a cryptic splice site, leading to the production of the toxic *Progerin* transcript that contains an in-frame deletion in exon 11. (C) Representative Western blot of tissue extracts from 9-month old $LMNA^{G609G/+}$ mice. 20 ug of protein loaded per lane. (D) Quantification of proportional Lamin A, Lamin C, and Progerin protein isoform abundance by Western blotting and densitometry in 9-month old $LMNA^{G609G/+}$ mice. *indicates that WAT was analyzed from 3-month-old animals because of the rapidly progressing lipodystrophy in these mice. (E) Lamin A/C absolute protein abundance (iBAQ) and *LMNA* RNA abundance (RNAseq FPKM) are very poorly correlated ($r^2 = 0$) across 29 human tissues. Data reanalyzed from Wang et al., *Mol Syst Biol* 2019. (F) Proportional abundance of *LMNA*, *LMNC*, and *Progerin* transcript abundance determined by digital droplet PCR in tissues from 9-month old $LMNA^{G609G/+}$ mice. *indicates that WAT was analyzed from 3-month-old animals. (G) Proportional abundance of *Progerin* transcript and Progerin protein are very poorly correlated across tissues from $LMNA^{G609G/+}$ mice.

Lamin A/C/Progerin protein and transcript levels are very poorly correlated across tissues

136 What other factors could modulate both the responsiveness of Progerin to treatment and
137 the effects of Progerin on a tissue? One potential influence could be the lifetime of the Lamin
138 A/C/Progerin proteins. A protein's lifetime reflects its rates of synthesis and degradation; short-
139 lived proteins are frequently renewed, while long-lived proteins can persist for weeks or even
140 months within mammalian tissues(*11*). Because long-lived proteins are rarely synthesized and
141 rarely degraded, their abundance may be poorly sensitive to changes in their transcript levels. To
142 explore the relationship between *LMNA* transcript and Lamin A/C protein abundance, we
143 compared tissue-matched RNAseq and proteomic data across 29 human tissues(*15*). This
144 analysis revealed that *LMNA* transcript and Lamin A/C protein abundances are uncorrelated (Fig.
145 1E, $r^2 \sim 0$). For comparison, the enzyme SYK has a high correlation between transcript and protein
146 levels across tissues(*15*) (Fig. S3, $r^2 = 0.89$). We next used digital droplet PCR to precisely
147 quantify the abundance of the *LMNA, LMNC,* and *Progerin* transcripts in progeroid mouse tissues
148 and observed that *Progerin* makes up a minor proportion of the transcripts produced from the
149 *LMNA* locus (Fig. 1F), yet these same tissues produce high levels of Progerin protein (Fig. 1C-
150 D). The proportional abundance of *Progerin* transcript and Progerin protein are thus very poorly
151 correlated (Fig. 1G). Taken together, these data indicate that Lamin A, Lamin C, and Progerin
152 protein levels are post-transcriptionally modulated in human and mouse tissues. Similarly poor
153 correlations between transcript and protein levels have been observed for extremely long-lived
154 proteins, such as components of the nuclear pore complex(*23*), leading us to speculate that Lamin
155 A/C and/or Progerin are also long-lived proteins.
156
157 ***Lamin A/C/Progerin are long-lived proteins in the cardiovascular system***
158
159 To test the hypothesis that the A-type Lamins have long lifetimes, we sought to determine
160 the turnover rates of these proteins within the tissues of healthy and progeroid mice. Proteome-
161 wide quantification of protein stability can be achieved *in vivo* by supplying mice with chow
162 containing the stable, non-toxic isotope ^{15}N, then tracking the rate of incorporation of ^{15}N-labeled
163 amino acids into the proteome over time by mass spectrometry(*14*, *24*). We recently used ^{15}N
164 metabolic labeling to profile trends in protein turnover across healthy mouse tissues(*14*), and here
165 applied the same 6-timepoint, 32-day labeling timecourse approach to age-matched *LMNA*$^{G609G/+}$
166 mice. These mice exhibit weight loss, bone abnormalities, atherosclerosis, and cardiac
167 dysfunction before succumbing to the disease between 9 and 12 months of age(*5*). We focused
168 our analyses on young adult mice at early stages of disease (9 to 12 weeks of age), and quantified
169 protein lifetimes in tissues that exhibit progeroid pathology (the aorta, heart, and white adipose

170 tissue) as well as tissues that are spared from disease (the intestine and liver). We defined protein
171 turnover rates (k_t) and corresponding predicted half-life ($t_{1/2}$) values for 2744 proteins in the large
172 intestine, 2098 proteins in the liver, 1881 proteins in the aorta, 1429 proteins in the white adipose
173 tissue, and 1608 proteins in the heart (Fig. S4A-B). Consistent with our previous analyses in
174 healthy tissues, proteins generally turn over more rapidly in the progeroid intestine (median $t_{1/2}$
175 1.6 days) and liver (median $t_{1/2}$ 2.7 days) than in the progeroid aorta (median $t_{1/2}$ 3.8 days), heart
176 (median $t_{1/2}$ 7.1 days) or fat (median $t_{1/2}$ 9.2 days).

177 While the goal of these experiments is to determine whether the A-type Lamins exhibit
178 variable lifetimes across tissues, a major confounding factor limits our ability to interpret
179 differences in protein lifetimes across tissues *in vivo*: the influence of cell turnover. That is, protein
180 turnover *in vivo* is shaped both by selective proteolytic degradation and non-selective dilution
181 during cell turnover. We recently developed a method, turnover and replication analysis by ^{15}N
182 isotope labeling (TRAIL) (Hasper et al 2022), to quantify both protein and cell lifetimes from the
183 same ^{15}N-labeled tissues to determine cell turnover-corrected protein degradation rates (Fig. 2A).
184 We applied this method to determine cell turnover rates (k_{div}) and doubling times within progeroid
185 intestine, liver, fat, and heart (Fig. S4C-D). (Cell turnover was not determined for the aorta due to
186 limited sample.) Overall, cell doubling times were similar in progeroid and healthy tissues with
187 one exception: the white adipose tissue, where progeroid cells had a doubling time of ~55 days
188 while age-matched wild type cells had a doubling time of ~78 days. This observation likely reflects
189 increased proliferation and/or increased death of adipocytes, which are the most abundant cell
190 type found in fat depots. Notably, over-expression of Progerin blocks the terminal differentiation
191 of adipocyte precursors(*25*), and HGPS patients suffer from severe lipodystrophy(*26*). We
192 speculate that *LMNA*$^{G609G/+}$ mice are in the early stages of lipodystrophy at 9 weeks of age, as
193 these animals are indistinguishable in weight compared to their littermates(*5*) (Fig. S5), although
194 their fat depots are moderately decreased in size.

195 By subtracting cell turnover rates (k_{div}) from protein turnover rates (k_t), we extrapolated cell
196 cycle-corrected protein degradation rates (k_{deg}) and predicted half-lives ($t_{1/2corr}$) for proteins in the
197 progeroid intestine, liver, heart, and fat. As we previously observed in wild type animals(*14*),
198 protein turnover rates vary widely across tissues even after cell cycle correction (Figure S4J-K).
199 We infer that the rate of cell division as well as environmental factors such as local metabolism
200 or the activity and selectivity of proteostasis networks shape protein lifetimes across tissues(*14*).
201 Global changes in protein stability are apparent in progeroid tissue, especially in the

Figure 2.

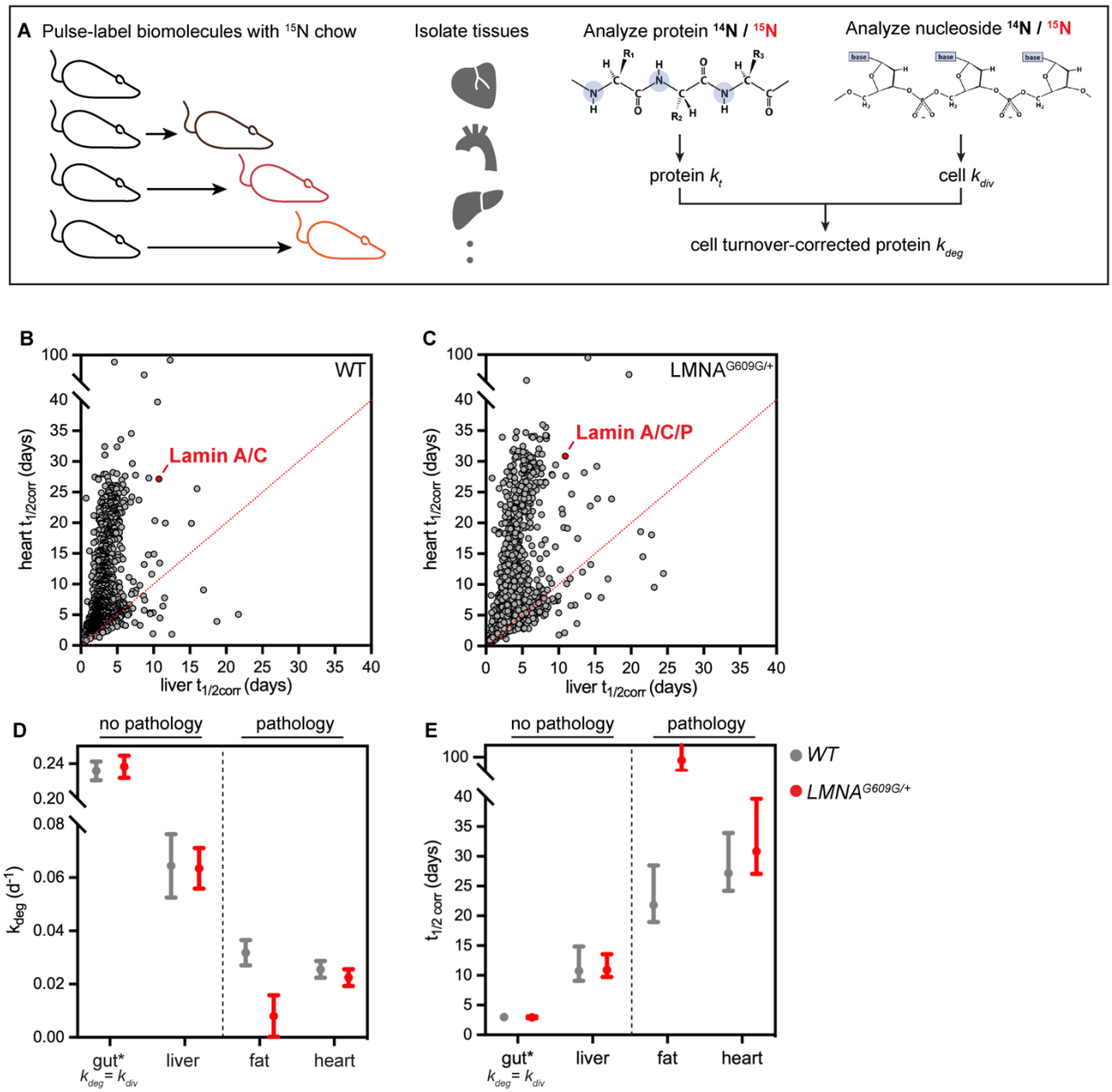

Figure 2. (A) Diagram of turnover and replication by ^{15}N isotope labeling (TRAIL) method for determining protein turnover (k_t) and cell turnover (k_{div}) by tracking ^{15}N incorporation into newly synthesized protein and genomic DNA, respectively. These two parameters are used to determine average bulk cell cycle-corrected protein degradation rates (k_{deg}). (B-C) Distribution of half-lives for proteins detected in both the liver and heart of healthy (B) and *LMNA*$^{G609G/+}$ (C) mice. The A-type Lamin proteins (red) are among a group of outliers with a dramatically longer lifetime in the heart than in the liver. (D-E) Cell cycle-corrected protein degradation rates (k_{deg}) (D) and half-lives ($t_{1/2corr}$) (E) for A-type Lamin proteins in tissues of healthy (gray) and *LMNA*$^{G609G/+}$ (red) mice. * denotes that A-type Lamin turnover is equivalent to cell turnover rate in the gut.

heart and fat, where the median protein half-life is extended by over a day compared to age-matched wild-type animals (Fig. S4K). At the individual protein level, 24-40% of quantified proteins have significantly extended lifetimes in progeroid tissues and are constituents of protein structures including mitochondria, ribosomes, the nucleus, and the cytoskeleton (Fig. S4F-I). Decreased

207 proteasome activity has been reported in fibroblasts derived from HGPS patients(*13, 27*), leading
208 us to speculate that decreased flux through the proteasome could underlie the extension of
209 protein lifetimes that we observe.

210 Within these shotgun proteomics experiments, we were able to determine the average
211 turnover behavior of the Lamin A, Lamin C, and Progerin proteins. We find that the A-type lamins
212 have highly variable lifetimes across both healthy and progeroid tissues. The distribution of half-
213 lives for proteins detected in both the liver and heart tissue of wild type (Fig. 2D) and progeroid
214 (Fig. 2E) animals illustrates this point, as the A-type lamins are among a small group of outlier
215 proteins that have a dramatically longer lifetime in the heart than in the liver. Overall, the lifetimes
216 of these proteins are longer in tissues that exhibit progeroid pathology (the aorta, heart, and fat)
217 compared to those that are spared from pathology (the liver and intestine) in both wild type and
218 progeroid animals (Table S3). After using TRAIL to quantify cell turnover rates and determine
219 corrected protein turnover rates, the differences between A-type lamin turnover flux across these
220 tissues were even more stark (Fig. 2D-E; cell turnover not determined for the aorta due to limited
221 sample); indicating that these proteins turn over dramatically more slowly in the fat and the heart.
222 After cell cycle correction, the predicted half-life for Lamin A/C in the healthy heart and fat is
223 approximately 3 weeks. Further, the average turnover rate of the closely related Lamin A, Lamin
224 C, and Progerin proteins is slowed to >1 month in the progeroid heart and fat compared to healthy
225 tissues, raising the possibility that the mutant Progerin protein turns over even more slowly than
226 wild type Lamin A/C (Table S3). However, we could not resolve isoform differences within these
227 data as the small subset of peptides that distinguish Lamin A, Lamin C, or Progerin from each
228 other were not detected.
229
230 ***Progerin exhibits impaired turnover and accumulates in the cardiovascular system***
231
232 Progerin retains a hydrophobic lipid modification that is only transiently present on wild-
233 type Lamin A(*28*), raising the possibility that this disease variant could be more aggregation-prone
234 and/or more recalcitrant to turnover than the normal protein. Lamin A is synthesized as a pre-
235 protein that matures through a series of post-translational modifications. These include a lipid
236 modification (farnesylation) followed by proteolytic cleavages that remove the lipid-modified C-
237 terminus to generate mature Lamin A(*29*). The HGPS mutation deletes a key protease cleavage
238 site(*28*), generating the constitutively farnesylated Progerin protein.

239 To determine whether the HGPS mutation extends protein lifetime, we
240 immunoprecipitated the A-type lamins from metabolically labeled progeroid heart, aorta, and liver

241 and performed parallel reaction monitoring mass spectrometry (PRM-MS)(*30*) to quantify
242 peptides unique to Lamin A *versus* Progerin (Fig. 3A-B). We did not monitor Lamin-C-only
243 peptides, as Lamin C is distinguishable from Lamin A only at its C-terminal 6 amino acids, and
244 this region does not generate any quantifiable and unique tryptic peptides. For maximum

Figure 3.

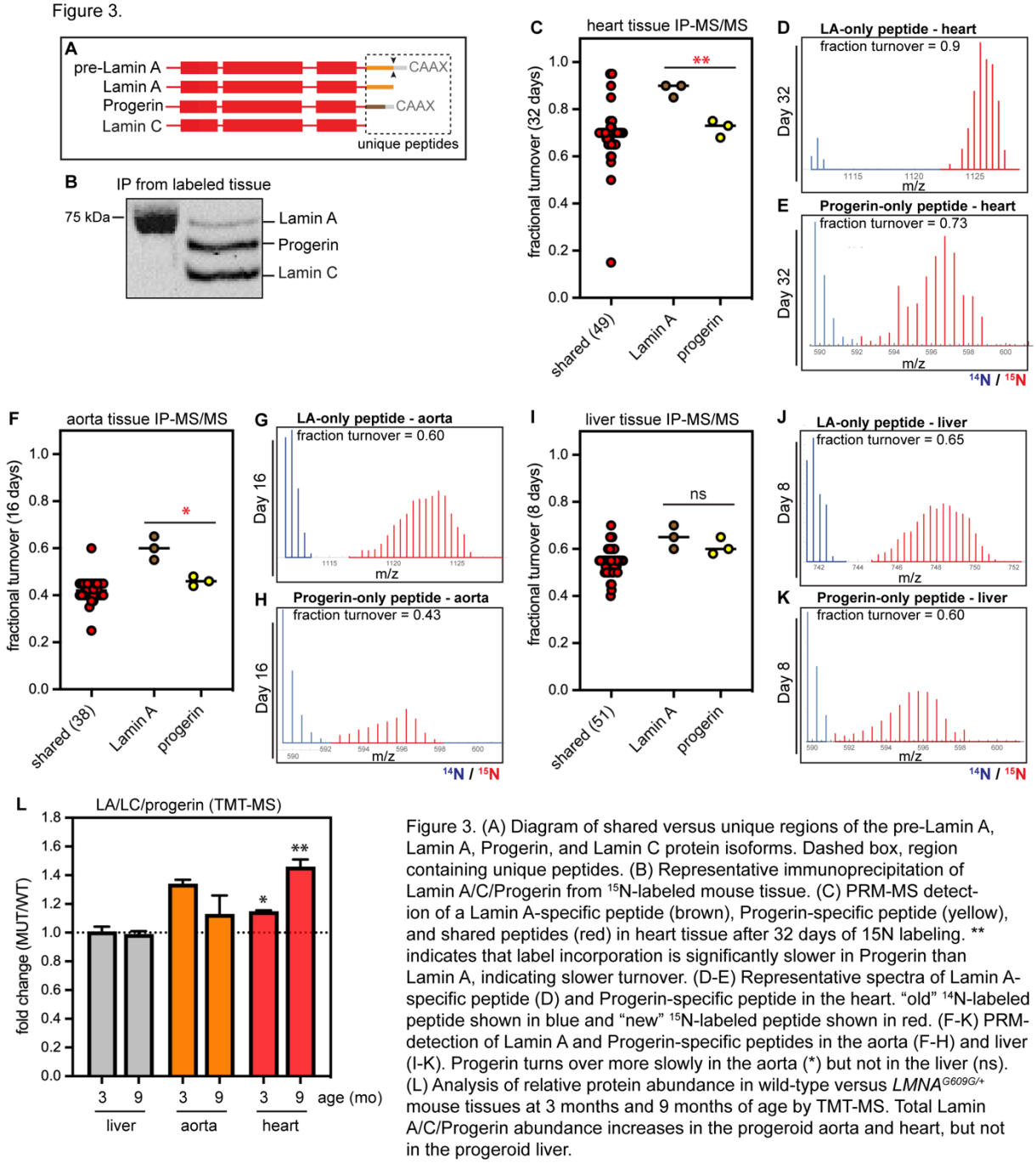

Figure 3. (A) Diagram of shared versus unique regions of the pre-Lamin A, Lamin A, Progerin, and Lamin C protein isoforms. Dashed box, region containing unique peptides. (B) Representative immunoprecipitation of Lamin A/C/Progerin from ^{15}N-labeled mouse tissue. (C) PRM-MS detection of a Lamin A-specific peptide (brown), Progerin-specific peptide (yellow), and shared peptides (red) in heart tissue after 32 days of 15N labeling. ** indicates that label incorporation is significantly slower in Progerin than Lamin A, indicating slower turnover. (D-E) Representative spectra of Lamin A-specific peptide (D) and Progerin-specific peptide in the heart. "old" ^{14}N-labeled peptide shown in blue and "new" ^{15}N-labeled peptide shown in red. (F-K) PRM-detection of Lamin A and Progerin-specific peptides in the aorta (F-H) and liver (I-K). Progerin turns over more slowly in the aorta (*) but not in the liver (ns). (L) Analysis of relative protein abundance in wild-type versus *LMNA*$^{G609G/+}$ mouse tissues at 3 months and 9 months of age by TMT-MS. Total Lamin A/C/Progerin abundance increases in the progeroid aorta and heart, but not in the progeroid liver.

245

246 sensitivity, we focused our analyses on the labeling timepoint that was closest to the predicted
247 half-life of the A-type lamins in each tissue: 32 days for the heart, 16 days for the aorta, and 8
248 days for the liver. By quantifying the $^{15}N/^{14}N$ isotope abundance ratio for individual peptides unique
249 to each protein isoform, we could compare the relative extent of turnover. These analyses
250 revealed that Progerin turns over significantly more slowly than wild type Lamin A in the heart
251 (Fig. 3C-E) and aorta (Fig. 3F-H) but not in the liver (Fig. 3I-K). Comparing these isoform-resolved
252 data to our bulk A-type lamin turnover data (Table I) leads us to estimate that Progerin's lifetime
253 within the cardiovascular system is on the order of months. Altogether, these protein turnover
254 analyses indicate that both tissue context and disease mutations modulate the lifetime of the A-
255 type lamin proteins.
256 If Progerin turnover is impaired compared to wild type Lamin A, one might predict that
257 Progerin would accumulate over time. We used tandem mass tagging (TMT) and proteomics(*31*)
258 to quantify relative protein abundance in healthy *versus* progeroid tissues from young adult mice
259 (3 months old) and from animals nearing the end of the HGPS mouse lifespan (9 months old).
260 These data indicated that the total dose of A-type lamin proteins is significantly increased in the
261 progeroid heart, but not the liver; while the dose of these proteins trends upward in the diseased
262 aorta, this trend is not significant due to variability across samples (Fig. 3L). Because this analysis
263 cannot distinguish Progerin from Lamin A, these data could indicate either that Progerin
264 accumulates over time, or that Progerin also interferes with the turnover of wild-type Lamin A,
265 leading to accumulation of all A-type lamin isoforms in diseased tissue. Altogether, these high-
266 resolution analyses reveal for the first time that Lamin A/C's lifetime is dramatically longer in
267 tissues that are vulnerable to laminopathy mutations, and that the turnover of the Progerin disease
268 variant is impaired only in the cardiovascular system, leading to protein accumulation over time.
269
270 ***Biochemical influences on Lamin A/C and Progerin protein lifetime***
271
272 Why are the A-type Lamins readily turned over in the liver, but more slowly turned over in
273 the heart? The lamins form head-to-tail filaments that bundle laterally(*32*) and stiffen(*33*) or
274 undergo structural changes(*34*) in response to mechanical force. Because the heart is a
275 contractile tissue under high strain, we hypothesized that differences in the folding and/or
276 assembly state of the Lamin proteins in the heart might underlie the proteins' longer lifetime in
277 this tissue. To test this hypothesis, we subjected tissue homogenates to sequential extractions of
278 increasing stringency - using salt, detergent, and denaturants(*35*) – and compared the extent of
279 Lamin A/C/Progerin extraction after each step. These analyses indicated that the A-type lamins

280 are poorly extractable in heart tissue, where complete extraction was possible only in strongly

Figure 4.

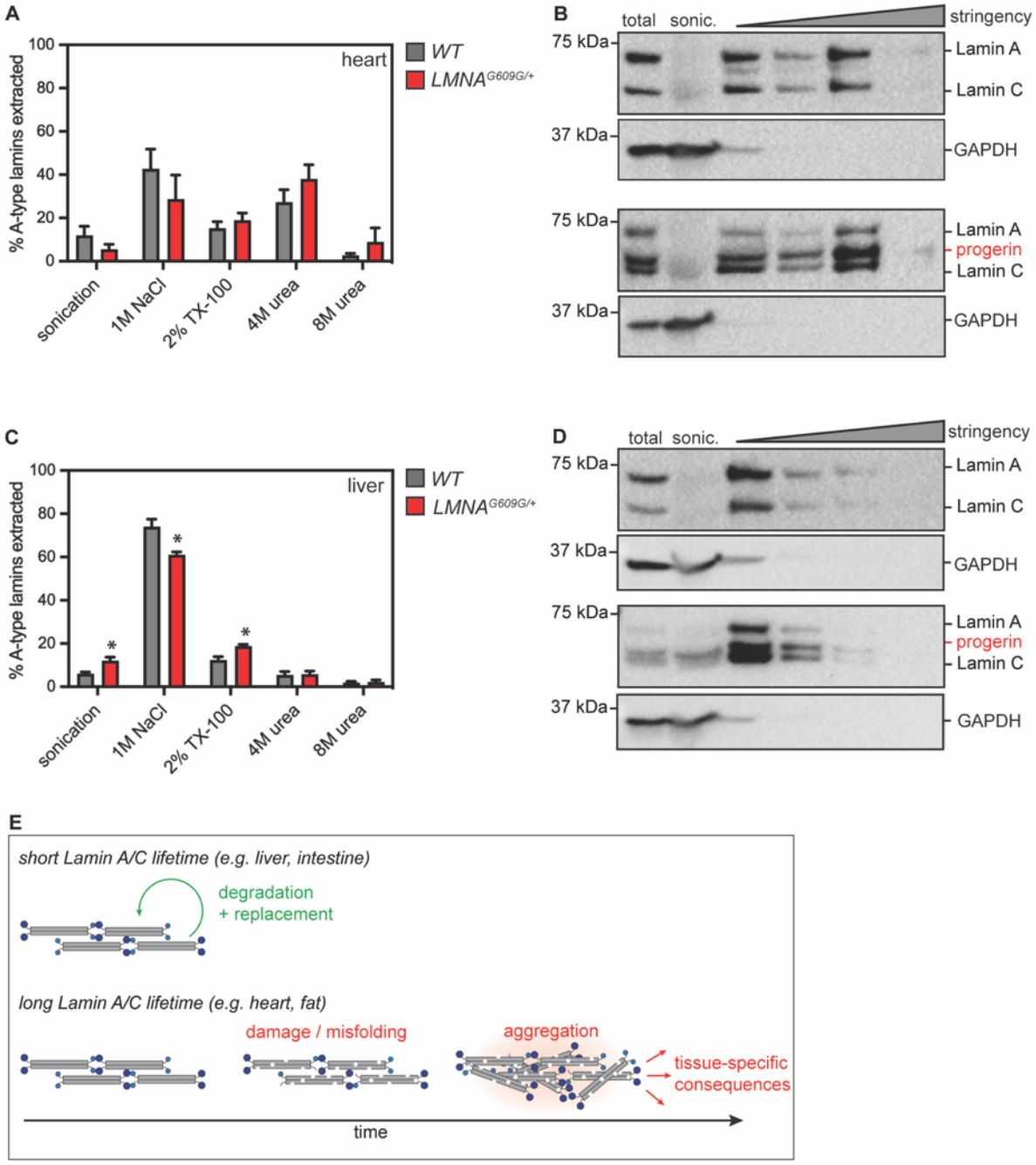

Figure 4. Serial extraction of LAmin A/C/Progerin proteins from heart (A-B) or liver (C-D) tissue of 4-month-old healthy and *LMNA*$^{G609G/+}$ mice. GAPDH indicates effective lysis and reelase of cytosol in each tissue. While Lamin A/C/Progerin are readily extractable with high salt in the liver (C-D) strong denaturants are required to completely extract these proteins from the heart (A). * indicates significant differences in protein solubility between wild type and *LMNA*$^{G609G/+}$ liver tissue. (E) Working model of interplay between protein turnover rate and time- and mutation-dependent accumulation of dysfunction in the progeroid cardiovascular system.

281

282 denaturing conditions (4M urea) (Fig. 4A-B). In the liver, in contrast, the A-type lamins were

283 efficiently extracted by treatment with high salt (Fig. 4C-D). These observations strongly imply

284 physicochemical differences in the assembly state of the Lamin polymers that correlate with the
285 differences in protein turnover rate between these tissues.

286 ***Human disease alleles are over-represented in the long-lived proteome***

287

288 Our data suggest that protein lifetime modulates the effects of disease-causative
289 mutations to cause tissue-specific disease. To explore the relationship between protein lifetime
290 and human disease more systematically, we evaluated the distributions of proteins linked to

Figure 5.

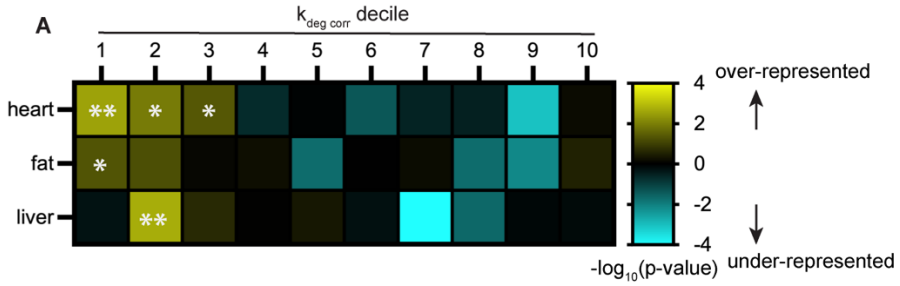

Table I. Long-lived proteins and human disease

Tissue	Name	Uniprot ID	k_{deg} (d^{-1})	$t_{1/2corr}$ (d)	Disease	OMIM
heart	CAV3	P51637	0.010 ± 0.003	68.9	Tateyama type distal myopathy	614321
					Familial hypertrophic cardiomyopathy	192600
					Long QT syndrome	611818
	ACTA1	P68134	0.016 ± 0.005	42.2	Nemaline myopathy	161800
	DYSF	Q9ESD7	0.024 ± 0.003	29.4	Limb-girdle muscular dystrophy	253601
					Miyoshi muscular dystrophy	254130
	LMNA	P48678	0.026 ± 0.003	26.7	Dilated cardiomyopathy	115200
					Emery-Dreifuss muscular dystrophy	616516
					Hutchinson-Gilford progeria syndrome	176670
					Congenital muscular dystrophy	613205
	DSG2	O55111	0.029 ± 0.005	24.0	Arrhythmogenic right ventricular dysplasia	610193
	ACTC1	P68033	0.031 ± 0.003	22.2	Left ventricular noncompaction	613424
					Hypertrophic cardiomyopathy	612098
					Atrial septal defect	612794
					Dilated cardiomyopathy, dilated	613424
fat	LMNA	P48678	0.032 ± 0.005	21.8	Familial partial lipodystrophy	151660
liver	KRT18	P05784	0.059 ± 0.012	11.7	Cryptogenic cirrhosis	215600
	AGL	F8VPN4	0.064 ± 0.008	10.9	Glycogen storage disease IIIa/IIIb	232400

Figure 5. (A) Analysis of distribution of human disease alleles (OMIM) across deciles of protein turnover rates in healthy mouse tissues. Map color indicates significance of over-representation (yellow) or under-representation (blue) of disease alleles in each decile. ** indicates that human disease alleles are significantly over-represented in the 1st, 2nd, and 3rd deciles of k_{deg} rate (most long-lived) in the heart; in the 1st decile in the fat; and in the 2nd decile in the liver (Fisher's exact test). Table II shows protein turnover rate data for selected long-lived proteins linked to human disease. Data re-analyzed from Hasper et al., BioRXiV 2022. See Table S4.

291

292 human disease across our recently acquired datasets of protein turnover rates in healthy mouse
293 heart, liver, and adipose tissues(*36*). We quantified the turnover rates of ~1600 to ~2100 proteins
294 per tissue, and found that mutations in ~600 to ~800 of those proteins are linked to human disease
295 in the OMIM database. Evaluating the distributions of these disease-linked proteins across
296 turnover rate deciles revealed that proteins linked to human disease are significantly over-
297 represented in the most long-lived proteins in each tissue – with the most dramatic over-
298 representation apparent in the heart (Fig. 5A, Table I, Table S4). Selected disease-linked proteins
299 found in the 1st decile of turnover rates in heart, liver, or fat are shown in Table I (see Table S4
300 for complete list). In addition to *LMNA,* mutations to *CAV3, ACTA1, ACTC1, DYSF,* and *DSG2*
301 are linked to cardiomyopathies and encode proteins that are long-lived in the heart. Some of these
302 proteins, such as ACTA1 and ACTC1, are selectively expressed in cardiac muscle, which
303 provides an obvious explanation for the tissue-specific consequences of mutations. However,
304 similarly to Lamin A/C, the DYSF, DSG2, and CAV3 proteins are expressed in several tissues but
305 are only long-lived in the heart (Fig. S6C-E), while the proteins KRT18 and AGL are broadly
306 expressed but are only long-lived in the liver (Fig. S6F-G), where their mutations cause disease.
307 These analyses overall reveal an unexpected enrichment of human disease alleles in extremely
308 long-lived proteins and suggest that protein lifetime may influence disease etiology not just in
309 laminopathies but also in other monogenetic human diseases.
310
311 **Discussion**
312
313 In this study, we applied quantitative proteomic approaches to explore the origins of tissue
314 specificity in laminopathy syndromes, which are caused by mutations to the abundant and broadly
315 expressed Lamin A/C protein. We determined that the Lamin A/C proteins have significantly
316 longer lifetimes within the cardiovascular system and fat, which are disrupted in laminopathies,
317 while these proteins have shorter lifetimes in disease-spared tissues such as the liver and
318 intestine. We demonstrated that the A-type Lamins are more densely bundled and less
319 extractable in the heart than in the liver. Since substrate unfolding is the major rate-limiting step
320 in protein degradation(*37*), more densely bundled Lamin polymers may be more recalcitrant to
321 protein turnover than the same proteins in a less densely bundled state. In the future, it will be
322 important to explore how Lamin assembly state modulates the functions of the nuclear lamina.
323 Our findings suggest that HGPS and other laminopathies may arise as a consequence of
324 disrupted proteostasis. In some tissues (such as the liver), the A-type Lamins may be maintained
325 in a folded and functional state by consistent degradation and replacement (Fig. 4E). In tissues

326 where the Lamins are long-lived (such as the heart), in contrast, protein synthesis and
327 degradation happen rarely. In this context, these long-lived proteins may undergo molecular
328 "aging" – meaning that they may accumulate damage, misfold, and perhaps irreversibly aggregate
329 in a time-dependent manner. Laminopathy-linked mutations may increase the propensity for
330 misfolding and/or irreversible aggregation over time, leading to the tissue-specific and time-
331 dependent accumulation of dysfunction. We found that the turnover of the HGPS-causative
332 Progerin mutant is selectively impaired within the cardiovascular system, leading to its
333 accumulation over time (Fig. 3). By analogy to neurodegenerative diseases caused by protein
334 aggregation(*38*), Progerin aggregates could act as a sink for the proteostasis machinery, with
335 global consequences on protein quality control. Indeed, we observe a significant slowdown in
336 general protein turnover flux in progeroid tissues (Figure S4).
337 All gene therapies rely on a key assumption: that targeting a gene or transcript will lead to
338 the desired changes to the encoded protein. We have demonstrated that Progerin is a long-lived
339 and toxic mutant protein. Because long-lived proteins are rarely synthesized and rarely degraded,
340 they are relatively insensitive to changes in their synthesis rate(*23*). This explains why gene
341 therapies have significant latency and limited potency in decreasing Progerin protein levels in the
342 cardiovascular system(*6*). Interestingly, combination treatment with a farnesyltransferase
343 inhibitor, which interferes with the biosynthesis of Progerin at the protein level, results in more
344 robust clearance of the mutant protein(*6*). Further exploration of orthogonal approaches for
345 interfering with Progerin protein production or accelerating protein degradation may identify new
346 therapies for this devastating disease.
347 By evaluating the relationship between human disease alleles and protein lifetime, we
348 discovered that disease-linked proteins are generally over-represented in the long-lived
349 proteome. As we have demonstrated in the context of HGPS, long protein lifetime may exert an
350 important influence on protein function and may present a major barrier to treatment in numerous
351 human disease states.
352
353
354 **Methods**
355 **Mouse model**
356 All animal experiments were performed in compliance with relevant ethical regulations and with
357 approval by the Institutional Animal Care and Use Committee at UCSF (IACUC protocol number
358 AN178187, PI: A.B.).
359

360 **Protein extraction from mouse tissues for Western blotting**

361 Approximately 30 milligrams of frozen tissue was excised on dry ice with a clean razorblade and
362 placed in a fresh tube. 100 uL of urea lysis buffer (ULB: 8M urea, 75 mM NaCl, 50 mM HEPES
363 pH 7.9, protease and phosphatase inhibitors) was added to the tube, and the tissue was then
364 minced on ice with scissors. ULB was added to a final volume of 600 uL, and the sample was
365 transferred to a Dounce homogenizer. The sample was homogenized for ~40 strokes with the
366 tight pestle, then transferred to a clean microcentrifuge tube. The sample was then probe
367 sonicated at 4C (10% amplitude, 10 seconds, 2 cycles) before being centrifuged (21,000 x g, 11
368 minutes, 4C). The supernatant was transferred to a clean tube. Protein concentration was
369 quantified by microBSA assay (Pierce). Lysates were mixed with SDS-PAGE sample buffer,
370 heated to 95°C for 5 minutes, and cooled. 20 micrograms of protein were loaded per well for
371 Western blot analysis and proteins were detected with an HRP-conjugated mouse monoclonal
372 antibody that recognizes an N-terminal epitope shared in Lamin A, Lamin C, and Progerin (Santa
373 Cruz sc-376248). Blots were visualized on a Chemi-Doc (BioRad) and proportional abundance of
374 each protein isoform was determined by densitometry.

375

376 **Serial extractions of protein from mouse tissues**

377 Relative solubility of the Lamin proteins was assayed using a serial extraction protocol adapted
378 from (*35*). Approximately 20 milligrams of frozen tissue was excised on dry ice with a clean
379 razorblade and placed in a fresh tube. Buffer 1 (10 mM HEPES pH 7.4, 2 mM MgCl2, 25 mM KCl,
380 250 mM sucrose, 1 mM DTT, protease and phosphatase inhibitors; 300 uL) was added to the
381 tube, and tissue was minced on ice. The sample was transferred to a Dounce homogenizer and
382 homogenized for ~40 strokes with the tight pestle, then transferred to a clean microcentrifuge
383 tube. The sample was probe sonicated at 4C (10% amplitude, 5 seconds, 2 cycles); a 50 uL
384 aliquot (whole tissue lysate) was retained. The remaining sample was then centrifuged (20,000 x
385 g, 5 minutes, 4C). The supernatant (S1) was retained. The pellet was resuspended in Buffer 2
386 (20 mM HEPES pH 7.4, 1 M NaCl, protease and phosphatase inhibitors; 250 uL) and incubated
387 20 minutes at RT with end-over-end rotation. The sample was then centrifuged (20,000 x g, 5
388 minutes, RT) and the supernatant (S2) was retained. The pellet was resuspended in Buffer 3 (20
389 mM HEPES pH 7.4, 1 M NaCl, 2% Triton-X-100, protease and phosphatase inhibitors; 250 uL)
390 and incubation and centrifugation were repeated. The supernatant (S3) was retained and the
391 pellet was resuspended in Buffer 4 (20 mM HEPES pH 7.4, 1M NaCl, 4M urea, protease and
392 phosphatase inhibitors; 250 uL) and incubation and centrifugation were repeated. Finally, the
393 supernatant (S4) was retained and the pellet was resuspended in Buffer 5 (20 mM HEPES pH

394 7.4, 1 M NaCl, 8M urea, protease and phosphatase inhibitors; 250 uL) and incubation and
395 centrifugation were repeated. The final supernatant (S5) was retained. An aliquot of the tissue
396 lysate and equal proportions of each supernatant were loaded on SDS-PAGE gels and processed
397 for Western blotting with an HRP-conjugated mouse monoclonal antibody that recognizes an N-
398 terminal epitope shared in Lamin A, Lamin C, and Progerin (Santa Cruz sc-376248).
399
400 **RNA extraction from mouse tissues**
401 Approximately 30 milligrams of frozen tissue was excised on dry ice with a clean razorblade and
402 placed in a fresh microcentrifuge tube. 100 uL of TRIzol was added, and tissue was minced with
403 scissors on ice. Additional TRIzol was added to a final volume of 500 uL and the sample was
404 transferred to a Dounce homogenizer. The sample was homogenized for ~40 strokes with the
405 tight pestle, then transferred to a clean microcentrifuge tube. The sample was incubated for 5
406 minutes at RT before chloroform (100 uL) was added. The sample was mixed by inversion and
407 incubated for 3 minutes, then centrifuged (12,000 x g, 15 minutes, 4C). The aqueous RNA-
408 containing supernatant was carefully removed and pipetted into a fresh tube. 1 uL of GlycoBlue
409 and 250 uL isopropanol were added to the supernatant, incubated for 10 minutes at RT, then
410 centrifuged (12,000 x g, 10 minutes, 4C). The supernatant was removed from the blue RNA-
411 glycogen pellet, then the pellet was resuspended in 500 uL 75% ethanol and centrifuged (7500 x
412 g, 5 minutes, 4C). The supernatant was removed and the pellet was allowed to air dry for 5-10
413 minutes. The pellet was resuspended in 50 uL nuclease-free water (Ambion) and RNA
414 concentration was determined by NanoDrop.
415
416 **Transcript quantification with digital droplet PCR**
417 For each sample, 1 ug of RNA was diluted into 15 uL reverse transcription reactions using the
418 iScript RT kit (Bio-Rad) and reactions were carried out following the manufacturer's instructions.
419 Each cDNA reaction was diluted to 10 ng/uL (RNA equivalents). For each sample, 20 ng (RNA
420 equivalents) was combined with 10 uL of 2x ddPCR Supermix for Probes (no UTP; Bio-Rad), 1
421 uL of a 20x FAM primer/probe set, 1 uL of a HEX primer/probe set, and nuclease free water to a
422 final volume of 20 uL. *Lmna* primers and probe sequences are listed below and are adapted
423 from(*6*). *mTfrc* primers and probe sequence was from Bio-Rad (PrimerPCR ddPCR Expression
424 Probe Assay for Tfrc Mouse (HEX)). Reaction droplets were generated on a Droplet Maker (Bio-
425 Rad); ddPCR reactions were run on a C1000 Thermocycler (Bio-Rad); and reactions were
426 analyzed on a QX100 ddPCR reader (Bio-Rad) according to the manufacturer's instructions.

427 ddPCR allows the absolute quantification of transcript abundance based on the ratio of positive
428 to negative droplets and is unaffected by primer-specific variables such as reaction efficiency(*39*).
429 We used absolute ddPCR quantification to determine the abundance of the *Lmna*, *Lmnc,* and
430 *Progerin* transcripts (copies per droplet). *mTfrc* reactions were run in the HEX channel of each
431 ddPCR reaction as a positive control, but were not used to normalize *Lmna* transcript
432 measurements. Transcript abundance was expressed as a proportion for each transcript. For
433 example, for *Lmna*:
434
435 proportional abundance *Lmna = [Lmna]/([Lmna] + [Lmnc] + [Progerin])*
436
437 ddPCR probe and primersets for mouse *Lmna, Lmnc,* and *Progerin* were as previously
438 described(*6*) and as listed in the following table.

Target	Primer (F)	Primer (R)	Probe
Lamin A (FAM)	ACCGCTCTCATCAACTCCAC	GCGGCGGCTGCCACTCAC	GGTTGAGGACAATGAGGATG
Progerin (FAM)	AGAAGAGCTCCTCCATCACC	ACATGATGCTGCAGTTCTGG	TGGAGCGGGAGCCCAGAGCTC
Lamin C (FAM)	ATCCATCTCCTCTGGCTCTT	ACATGATGCTGCAGTTCTGG	TCCAGTCCCCGGAGCCAG/AGCT

439
440 **Metabolic labeling of mice and tissue isolation**
441 As recently described(*14*), we performed a 6-timepoint, 32-day ^{15}N labeling timecourse (0, 2, 4,
442 8, 16, and 32 days of labeling) with a total of 3 animals of both sexes per labeled timepoint, and
443 2 animals for the day 0 (unlabeled) timepoint. Timecourses were performed in *LMNA*$^{G609G/+}$
444 C57Bl/6 mice at approximately 9 weeks of age. ^{14}N and ^{15}N mouse chow was obtained from
445 Silantes. Animals were first habituated to the chow formulation by feeding ^{14}N (normisotopic) food
446 for 1 week; animals were then transitioned to ^{15}N chow throughout the labeling period (roughly 3
447 grams / animal / day). Animals were sacrificed by CO_2 inhalation followed by cervical dislocation,
448 followed by tissue dissection and flash freezing by submersion in liquid nitrogen.
449
450 **Protein extraction and sample preparation for LC-MS/MS**
451 *Protein extraction:* Approximately 30 milligrams of frozen tissue was excised on dry ice with a
452 clean razorblade and placed in a fresh tube. 100 uL of protein extraction buffer (PEB: 5% SDS,
453 100 mM TEAB, protease and phosphatase inhibitors, pH ~7) was added to the tube. The tissue
454 was minced on ice; PEB was added to bring the final volume to 600 uL, then the sample was
455 transferred to a Dounce homogenizer. The sample was homogenized for ~40 strokes with the
456 tight pestle, then transferred to a clean microcentrifuge tube. The sample was then probe
457 sonicated at 4C (10% amplitude, 10 seconds, 2 cycles) before being centrifuged (21,000 x g, 11

458 minutes, 4C). The supernatant was transferred to a clean tube, and aliquots were separated for
459 proteomics and protein quantification by microBSA assay (Pierce).

460 *Trypsinization:* Samples were diluted to 1 mg/mL in 5% SDS, 100 mM TEAB, and 25 µg of protein
461 from each sample was reduced with dithiothreitol to 2 mM, followed by incubation at 55°C for 60
462 minutes. Iodoacetamide was added to 10 mM and incubated in the dark at room temperature for
463 30 minutes to alkylate proteins. Phosphoric acid was added to 1.2%, followed by six volumes of
464 90% methanol, 100 mM TEAB. The resulting solution was added to S-Trap micros (Protifi), and
465 centrifuged at 4,000 x g for 1 minute. The S-Traps containing trapped protein were washed twice
466 by centrifuging through 90% methanol, 100 mM TEAB. 1 µg of trypsin was brought up in 20 µL of
467 100 mM TEAB and added to the S-Trap, followed by an additional 20 µL of TEAB to ensure the
468 sample did not dry out. The cap to the S-Trap was loosely screwed on but not tightened to ensure
469 the solution was not pushed out of the S-Trap during digestion. Samples were placed in a humidity
470 chamber at 37°C overnight. The next morning, the S-Trap was centrifuged at 4,000 x g for 1
471 minute to collect the digested peptides. Sequential additions of 0.1% TFA in acetonitrile and 0.1%
472 TFA in 50% acetonitrile were added to the S-trap, centrifuged, and pooled. Samples were frozen
473 and dried down in a Speed Vac (Labconco) prior to TMTpro labeling.

474 *TMT labeling*: Samples were reconstituted in TEAB to 1 mg/mL, then labeled with TMTpro 16plex
475 reagents (Thermo Fisher) following the manufacturers protocol. Briefly, TMTpro tags were
476 removed from the -20°C freezer and allowed to come to room temperature, after which acetonitrile
477 was added. Individual TMT tags were added to respective samples and incubated at room
478 temperature for 1 hour. 5% hydroxylamine was added to quench the reaction, after which the
479 samples for each experiment were combined into a single tube. Since we performed abundance
480 quantitation on unlabeled peptides, 0 day samples were added to four of the unused channels,
481 increasing the signal for the unlabeled peptides. TMTpro tagged samples were frozen, dried down
482 in the Speed Vac, and then desalted using homemade C18 spin columns to remove excess tag
483 prior to high pH fractionation.

484 *High pH Fractionation:* Homemade C18 spin columns were activated with two 50 µL washes of
485 acetonitrile via centrifugation, followed by equilibration with two 50 µL washes of 0.1% TFA.
486 Desalted, TMTpro tagged peptides were brought up in 50 µL of 0.1% TFA and added to the spin
487 column. After centrifugation, the column was washed once with water, then once with 10 mM
488 ammonium hydroxide. Fractions were eluted off the column with centrifugation by stepwise
489 addition of 10 mM ammonium hydroxide with the following concentrations of acetonitrile: 2%,

490 3.5%, 5%, 6.5%, 8%, 9.5%, 11%, 12.5%, 14%, 15.5%, 17%, 18.5%, 20%, 21.5%, 27%, and 50%.
491 The sixteen fractions were concatenated down to 8 by combining fractions 1 and 9, 2 and 10, 3
492 and 11, etc. Fractionated samples were frozen, dried down in the Speed Vac, and brought up in
493 0.1% TFA prior to mass spectrometry analysis.

494 **LC-MS/MS Analysis**

495 *Data collection:* Peptides from each fraction were injected onto a homemade 30 cm C18 column
496 with 1.8 um beads (Sepax), with an Easy nLC-1200 HPLC (Thermo Fisher), connected to a Fusion
497 Lumos Tribrid mass spectrometer (Thermo Fisher). Solvent A was 0.1% formic acid in water,
498 while solvent B was 0.1% formic acid in 80% acetonitrile. Ions were introduced to the mass
499 spectrometer using a Nanospray Flex source operating at 2 kV. The gradient began at 3% B and
500 held for 2 minutes, increased to 10% B over 7 minutes, increased to 38% B over 94 minutes, then
501 ramped up to 90% B in 5 minutes and was held for 3 minutes, before returning to starting
502 conditions in 2 minutes and re-equilibrating for 7 minutes, for a total run time of 120 minutes. The
503 Fusion Lumos was operated in data-dependent mode, employing the MultiNotch Synchronized
504 Precursor Selection MS3 method to increase quantitative accuracy(*40*). The cycle time was set
505 to 3 seconds. Monoisotopic Precursor Selection (MIPS) was set to Peptide. The full scan was
506 done over a range of 400-1500 m/z, with a resolution of 120,000 at m/z of 200, an AGC target of
507 4e5, and a maximum injection time of 50 ms. Peptides with a charge state between 2-5 were
508 picked for fragmentation. Precursor ions were fragmented by collision-induced dissociation (CID)
509 using a collision energy of 35% and an isolation width of 1.0 m/z. MS2 scans were collected in
510 the ion trap with an AGC target of 1e4 and a maximum injection time of 35 ms. MS3 scans were
511 performed by fragmenting the 10 most intense fragment ions between 400-2000 m/z, excluding
512 ions that were 40 m/z less and 10 m/z greater than the precursor peptide, using higher energy
513 collisional dissociation (HCD). MS3 ions were detected in the Orbitrap with a resolution of 50,000
514 at m/z 200 over a scan range of 100-300 m/z. The isolation width was set to 2 Da, the collision
515 energy was 60%, the AGC was set to 1e5, and the maximum injection time was set to 100 ms.
516 Dynamic exclusion was set to 45 seconds.

517 *Data analysis*: Raw data was searched using the SEQUEST search engine within the Proteome
518 Discoverer software platform, version 2.4 (Thermo Fisher), using the Uniprot mouse database
519 (downloaded January 2020). Trypsin was selected as the enzyme allowing up to 2 missed
520 cleavages, with an MS1 mass tolerance of 10 ppm, and an MS2 mass tolerance of 0.6 Da.
521 Carbamidomethyl on cysteine, and TMTpro on lysine and peptide N-terminus were set as a fixed

522 modifications, while oxidation of methionine was set as a variable modification. Percolator was
523 used as the FDR calculator, filtering out peptides which had a q-value greater than 0.01. Reporter
524 ions were quantified using the Reporter Ions Quantifier node, with an integration tolerance of 20
525 ppm, and the integration method being set to "most confident centroid". Protein abundances were
526 calculated by summing the signal to noise of the reporter ions from each identified peptide, while
527 excluding any peptides with an isolation interference of greater than 30%, or SPS matches less
528 than 65%.

529 *Kinetic model:* The kinetic model applied in this study has been previously described(*41*). Briefly,
530 we are assuming that protein synthesis is a zero order process, occurs at a constant fractional
531 rate, and that that the total protein concentration of each cell does not change during the
532 experimental time-course. The dilution of the protein pool due to cell division can be modeled as
533 a first order exponential process. Thus, the fractional turnover of unlabeled proteins during the
534 labeling time course can be regarded as a first order kinetic process that can be modelled based
535 on the following exponential equation:

536 $$\text{fraction unlabeled protein}(t) = e^{-k_t * t} \quad (1)$$

537 And:

538 $$k_t = k_{deg} + k_{div}$$

539 Where:

540 k_t is the clearance rate (observed rate of fractional labeling), k_{deg} is the rate of protein
541 degradation and k_{div} is the rate of cell division.

542 The determination of k_t values were conducted as previously described(*41*) using the decay of
543 the TMT reporter signals of unlabeled proteins. Protein-level TMT reporter abundances for
544 unlabeled proteins for each replicate experiment were first normalized by dividing by the intensity
545 of the t0 reporter and then the replicate experiments were aggregated in a single kinetic curve. In
546 fitting the exponential decay curves of the unlabeled protein signals, a constant fractional baseline
547 at infinite time was incorporated in the fitting equation. The equation used for fitting the curves
548 was therefore: $intensity = baseline + (1 - baseline) * e^{-k_t * time}$. The goodness of fit for least
549 squares fits were assessed by determining the R^2, P-value and t-statistic of the fits (see Supp

550 Table 1). For subsequent analyses, only protein k_t measurements that were obtained from all
551 three replicate experiments, incorporated data from 4 or more peptide spectral matches (PSMs),
552 and had t-statistic values greater than three were considered.

553 **Nucleic acid extraction and sample preparation for LC-MS/MS**

554 *Genomic DNA extraction:* Approximately 30 milligrams of frozen tissue was excised on dry ice
555 with a clean razorblade and placed in a fresh tube. 100 uL of TRIzol reagent (Invitrogen) was
556 added and the tissue was rapidly minced on ice. An additional 400 uL of TRIzol was added, and
557 the sample was then transferred to a Dounce homogenizer. The tissue was subjected to ~40
558 strokes with the tight pestle until smooth, then transferred back to the original tube. The sample
559 was incubated for at least 5 minutes before the addition of 100 uL chloroform followed by mixing
560 and a further 3 minutes of incubation. The sample was then centrifuged (12,000 x g, 15 minutes,
561 4C) and the upper RNA-containing aqueous layer was discarded. 150 uL of absolute ethanol was
562 added to the remaining sample, then inverted several times to mix. After 3 minutes of incubation
563 at room temperature, the sample was centrifuged (2,000 x g, 5 minutes, 4C). The protein-
564 containing supernatant was removed, then the DNA-containing pellet was resuspended in 500 uL
565 of absolute ethanol and incubated for 30 minutes. The sample was then centrifuged (2,000 x g, 5
566 minutes, 4C), and the supernatant discarded. Sequential washes were then repeated with 95%,
567 85%, and 75% ethanol, after which the pellet was air-dried for 5-10 minutes. The pellet was then
568 resuspended in 200 uL nuclease-free water (Ambion) at 56C, then incubated at 56C with shaking
569 for 30 minutes to resuspend the pure DNA. The sample was centrifuged (12,000 x g, 10 minutes,
570 4C), then the supernatant containing pure DNA was moved to a clean tube. DNA concentration
571 was determined with a NanoDrop spectrophotometer.
572
573 *Digestion of genomic DNA to short oligonucleotides:* 3-5 micrograms of pure genomic DNA was
574 diluted to a 50 uL volume in nuclease-free water, then combined with 50 uL of 2x Dinucleotide
575 Buffer (DB: 5 mU/uL benzonase, 40 mU/uL shrimp alkaline phosphatase, 20 mM Tris pH 7.9, 100
576 mM NaCl, 20 mM MgCl2). Samples were incubated overnight at 37C. Spin-X UF Concentrators
577 (Corning) were rinsed with 200 uL buffer (20 mM Tris pH 7.9, 100 mM NaCl, 20 mM MgCl2), then
578 samples were applied and centrifuged through (12,000 x g, 5 min, RT). The eluate was collected
579 for analysis.
580
581 *Digestion of genomic DNA to mononucleosides:* We extracted mononucleosides from genomic
582 DNA similarly to a previously described method(*42*) with some modifications. 1-3 micrograms of

583 pure genomic DNA was diluted to a 50 uL volume in nuclease-free water, then combined with 50
584 uL of 2x Mononucleoside Buffer (MB: 5 mU/uL benzonase, 40 mU/uL shrimp alkaline
585 phosphatase, 60 uU/uL phosphodiesterase I, 20 mM Tris pH 7.9, 100 mM NaCl, and 20 mM
586 MgCl2). Samples were incubated overnight at 37C. Spin-X UF Concentrators (Corning) were
587 rinsed with 200 uL buffer (20 mM Tris pH 7.9, 100 mM NaCl, 20 mM MgCl2), then samples were
588 applied and centrifuged through (12,000 x g, 5 min, RT). The eluate was collected for analysis.
589
590 **Mononucleoside and Dinucleotide LC-MS/MS**

591 Mononucleoside analyses were carried out by adapting a previously described method(*43*) using
592 a Dionex Ultimate 3000 UHPLC coupled to a Q Exactive Plus mass spectrometer (Thermo
593 Scientific). After purification, analytes were separated on a Hypersil Gold 2.1 x 150 mm column,
594 protected by a 2.1 x 10 mm Hypersil Gold guard column (Thermo Scientific). The mobile phases
595 were A: 0.1% formic acid in water, and B: 0.1% formic acid in acetonitrile. The flow rate was set
596 to 400 µL/min, and the column oven was set to 36°C. 10 µL of each sample was injected, and the
597 analytes were eluted using the following gradient: 0 min- 0% B, 6 min- 0% B, 8.5 min- 80% B, 9.5
598 min- 80% B, 10 min- 0% B, 13 min- 0% B. The Q Exactive Plus was operated in positive mode
599 with a heated electrospray ionization (HESI) source. The spray voltage was set to 3.5 kV, the
600 sheath gas flow rate was set to 40, and the auxiliary gas flow rate set to 7, while the capillary
601 temperature was set to 320°C. A parallel reaction monitoring (PRM) method was used to quantify
602 the unlabeled nucleotide, along with all of its N15 isotopes in a single scan. This was
603 accomplished by using wide (8 m/z) isolation widths when selecting the nucleotides for
604 fragmentation. By employing this method, we were able to quantify the level of labeling by looking
605 at the intensity of each N15 labeled base in the MS2 scan. Fragment ions were detected in the
606 Orbitrap with a resolution of 70,000 at m/z 200. Using a high resolution MS2 scan allowed us to
607 resolve N15 and C13 isotopes. Peak areas from the fragment ions were extracted with a 10 ppm
608 mass tolerance using the LC Quan node of the XCalibur software (Thermo Scientific).

609 Dinucleotide analyses were carried out using the same instrumentation, column, mobile phases,
610 column temperature, and flow rate employed by the mononucleoside experiments. The gradient
611 was changed to optimize dinucleotide separation as follows: 0 min- 5% B, 0.5 min- 5% B, 2.5 min-
612 90% B, 3.25 min- 90% B, 3.5 min- 5% B, 5.5 min- 5% B. The Q Exactive Plus was operated using
613 the same tune settings as the mononucleotide experiment. However, instead of a PRM method,
614 a full scan method from 500-650 m/z was developed to quantify the dinucleotides dCdC, TT,
615 dAdA, and dGdG, along with their corresponding N15 isotopes. Precursor ions were detected in

616 the Orbitrap with a resolution of 140,000 at m/z 200, using the high resolution MS1 scan to try to
617 separate N15 and C13 isotopes as much as possible. Peak areas from the fragment ions were
618 extracted with a 10 ppm mass tolerance using the LC Quan node of the XCalibur software
619 (Thermo Scientific).

620 *Measurement of kdiv*

621 To accurately measure rates of cell division (k_{div}) while factoring in the effects of incomplete
622 labeling and nucleotide recycling, we considered the time-dependent labeling patterns of
623 mononucleosides derived from genomic DNA. Upon initiation of ^{15}N labeling, newly synthesized
624 DNA strands can incorporate nucleotides from a precursor pool that includes fully ^{15}N-labeled
625 nucleotides derived from the dietary source, partially labeled species (containing one to four ^{15}N
626 atoms) derived by biosynthesis from incompletely labeled ^{15}N precursors, and completely
627 unlabeled nucleotides derived from recycling. Therefore, it may not be possible to accurately
628 determine the ratio of new to old strands (and hence k_{div}) from the mononucleotide data alone.
629 We previously used the labeling pattern of dinucleotides to resolve this ambiguity(*14*). The
630 isotopologue distribution of labeled (non-monoisotopic) peaks in the dinucleotide spectra are
631 dependent on the composition of the nucleotide precursor pool. Through regression analyses, we
632 determined that within all tissues and timepoints analyzed in this study, the isotopologue
633 distributions of the dinucleotide data could be best modeled based on the assumption that newly
634 synthesized strands had very low levels of fully unlabeled nucleotides. Hence, the fractional
635 population of labeled non-monoisotopic peaks within dinucleotide and mononucleotide data were
636 consistent with each other and could be used to determine the fractional population of new
637 strands. For each tissue, fractional labeling of mononucleotide and dinucleotides for all 4 bases
638 were combined and the aggregated dataset was fit to a single exponential equation to determine
639 first order rate constant for division (k_{div}). These data appear in Table S2.
640

641 **Analysis of Proteomic Data**

642

643 *Quality filtering and analysis of k_t values:* Proteomic data was acquired in the form of 16-plex TMT
644 replicates containing 2 full 6-timepoint timecourses (one from wild type animals and one from
645 progeroid animals). For each genotype within each TMT replicate, proteins were filtered to retain
646 only those detected with at least 3 peptide spectral matches (PSMs) in all timepoints. Proteins
647 that met these criteria were then filtered per genotype within each TMT replicate based on
648 goodness of fit using the t-statistic. The t-statistic is equal to the turnover rate (k_t) divided by the

649 standard error of that value. This metric determines to what extent measurement error influences
650 k_t. We applied a minimum t-statistic cutoff of 3, meaning that the magnitude of the turnover rate
651 k_t is at least 3 times the magnitude of the standard error. Between 50% to 63% of detected proteins
652 passed these coverage and goodness-of-fit criteria (Figure S2). Along with the sample size, the
653 t-statistic can be used to determine a p-value that indicates the probability that the turnover rate
654 reported has a meaningful non-zero value. The k_t, standard error, t-statistic, and p-value for each
655 protein are reported in Table S1. The k_t, standard error, and sample size were used to perform
656 per-protein statistical tests across tissues, to identify proteins with significantly different turnover
657 kinetics between tissues. These data are reported in Table S1.
658
659 *Determination of relative protein abundance within tissues*: To evaluate relative protein
660 abundance between genotypes within tissues of 3-month-old mice, technical replicate unlabeled
661 wild type and progeroid samples from each multiplexed TMT run were first channel normalized,
662 then the geometric mean was calculated to determine mean normalized intensities for each
663 biological replicate. Protein abundance was then length-normalized by dividing each protein's
664 normalized intensity by the number of amino acids. Finally, samples were normalized for
665 comparison across biological replicates by normalizing each channel to the maximum value
666 detected. The geometric mean abundance across all biological replicates was calculated by
667 determining the geometric mean of the length- and channel-normalized protein abundance.
668 Finally, the fold change of protein abundances between wild type and progeroid tissues was
669 determined.
670
671 Additional multiplexed TMT experiments were performed to compare protein abundances within
672 tissues from 9-month-old wild type and progeroid mice. In these experiments, two biological
673 replicate samples were analyzed in technical duplicate for each genotype in an 8-plex TMT
674 experiment per tissue. Raw data were subjected to the same sequence of technical replicate
675 averaging, protein length normalization, channel normalization, biological replicate averaging,
676 and fold change determination described above.
677
678 *Identification of disease-linked proteins:* Disease associations were determined by cross-
679 referencing proteomic datasets to the Online Mendelian Inheritance in Man (OMIM) database
680 (www.omim.org). A complete list of OMIM allele – gene associations for the mouse genome was
681 downloaded from OMIM, then cross-referenced to mouse proteins in each decile of turnover rate,

682 ranging from 1st decile (most long-lived) to 10th decile (most short-lived) in each tissue. Over-
683 representation of disease alleles in deciles was evaluated by Fisher's exact test.
684
685 **Protein immunoprecipitation from mouse tissues**
686 Metabolically labeled tissue extracts from progeroid animals prepared as described above in PEB
687 for proteomic analysis were used for immunoprecipitation as follows. Approximately 1300-1500
688 ug of lysate (100 uL) was aliquoted into a fresh tube and diluted to 2 mL final volume in Dilution
689 Buffer (10 mM Tris pH 7.4, 150 mM NaCl, 1% Triton-X-100, 1% deoxycholate, 2.5 mM MgCl2,
690 protease and phosphatase inhibitors). For each sampe, 60 uL of Protein G magnetic beads (Life
691 Technologies) were rinsed and resuspended in Dilution Buffer, then added to the diluted lysate.
692 The sample was incubated at 4C with rotation for 30 minutes. Beads were removed and the pre-
693 cleared supernatant was transferred to a clean tube; 5% of the sample was reserved as input. A
694 mixture of two anti-Lamin A/C antibodies was used to immunoprecipitated Lamin A, Lamin C, and
695 Progerin: Lamin A/C E-1 (Santa Cruz sc-376248, 20 uL per IP) and Lamin A/C (Active Motif
696 #39288 Clone 3A6-4C11, 5 uL per IP). The IP was incubated overnight at 4C with nutation. 60 uL
697 of pre-rinsed Protein G beads were then added to the sample and incubated for 30 minutes at 4C
698 with nutation. Beads were collected on a magnetic stand and supernatant (flow-through) was
699 saved in a fresh tube. Beads were washed in 3 x 1 mL of Wash Buffer (10 mM Tris pH 7.4, 150
700 mM NaCl, 0.5 mM EDTA, 0.1% SDS, 1% Triton-X-100, 1% deoxycholate, 2.5 mM MgCl2,
701 protease and phosphatase inhibitors). Following the third wash, liquid was carefully removed
702 using a gel loading tip; 2x SDS-PAGE sample buffer was added to the beads, and proteins were
703 eluted by boiling for 5 minutes at 95C.
704 To check the efficiency of each IP, equal proportions of the input and flow-through
705 fractions were analyzed by Western blotting for Lamin A/C (E-1 HRP, Santa Cruz, sc-376248
706 HRP). If a noticeable decrease in protein abundance was apparent in the flow-through sample,
707 the IP samples were run on an SDS-PAGE gel and stained with Colloidal Coomassie stain. A gel
708 slice containing the Lamin A, Lamin C, and Progerin bands was cut out for downstream mass
709 spectrometry analysis.
710
711 **SIM/PRM-MS of Lamin and Progerin peptides**

712 *Data collection:* SIM/PRM was performed as described above with the following changes. The
713 gradient began at 3% B and held for 2 minutes, increased to 10% B over 5 minutes, increased to
714 38% B over 38 minutes, then ramped up to 90% B in 3 minutes and was held for 3 minutes, before

715 returning to starting conditions in 2 minutes and re-equilibrating for 7 minutes, for a total run time
716 of 60 minutes. The Fusion Lumos was operated using dual experiments, the first being a tSIM
717 scan and the second being a PRM scan. Each tSIM scan targeted ions with an m/z of 597.7463
718 using an isolation window of 20 m/z, covering the range of the unique Progerin peptide and all
719 possible N15 isotopes. The resolution was set to 120,000 at m/z of 200, an AGC target of 1e5,
720 and a maximum injection time of 246 ms. The PRM scan fragmented precursor ions with an m/z
721 of 589.7463 by collision-induced dissociation (CID) using a 1.6 m/z isolation width. The collision
722 energy was set to 30% with a maximum injection time of 250 ms, and an AGC target of 1e4. The
723 Ion Trap Scan Rate was set to 'Rapid'.

724 *Data analysis*: The presence of Progerin was validated using raw MS2 data. Raw SIM data were
725 searched for precursor ions with an m/z of 589.7463 and z of 2 in addition to all possible N15
726 isotopologues. The intensity of each isotopologue was measured using Thermo XCalibur Qual
727 Browser (Table S5).
728

729 **Data Availability**

730 LC-MS/MS data have been deposited in the ProteomeXchange Consortium via the PRIDE partner
731 repository, accessible at www.ebi.ac.uk/pride. The accession codes will be included in the final
732 manuscript.
733

734 **Author Contributions**

735

736 J.Hasper and A.B. performed in vivo labeling experiments, tissue isolations, and protein and DNA
737 extractions. J. Hryhorenko and K. W. prepared and ran samples for LC-MS/MS. A.B., J.Hasper,
738 K.W., and S.G. analyzed data. A.B. and J. Hasper prepared the figures. A.B. wrote the
739 manuscript.
740

741 **References**

742

743 1. K. H. Schreiber, B. K. Kennedy, When Lamins Go Bad: Nuclear Structure and Disease. *Cell*.
744 152, 1365–1375 (2013).

745 2. O. Santiago-Fernández, F. G. Osorio, V. Quesada, F. Rodríguez, S. Basso, D. Maeso, L.
746 Rolas, A. Barkaway, S. Nourshargh, A. R. Folgueras, J. M. P. Freije, C. López-Otín,
747 Development of a CRISPR/Cas9-based therapy for Hutchinson–Gilford progeria syndrome. *Nat*
748 *Med*. 25, 423–426 (2019).

749 3. E. Beyret, H.-K. Liao, M. Yamamoto, R. Hernandez-Benitez, Y. Fu, G. Erikson, P. Reddy, J.
750 C. I. Belmonte, Single-dose CRISPR–Cas9 therapy extends lifespan of mice with Hutchinson–
751 Gilford progeria syndrome. *Nature Medicine*, 1–14 (2019).

752 4. L. W. Koblan, M. R. Erdos, C. Wilson, W. A. Cabral, J. M. Levy, Z.-M. Xiong, U. L. Tavarez, L.
753 M. Davison, Y. G. Gete, X. Mao, G. A. Newby, S. P. Doherty, N. Narisu, Q. Sheng, C. Krilow, C.
754 Y. Lin, L. B. Gordon, K. Cao, F. S. Collins, J. D. Brown, D. R. Liu, In vivo base editing rescues
755 Hutchinson– Gilford progeria syndrome in mice. *Nature*, 1–30 (2021).

756 5. F. G. Osorio, C. L. Navarro, J. Cadiñanos, I. C. López-Mejía, P. M. Quirós, C. Bartoli, J.
757 Rivera, J. Tazi, G. Guzmán, I. Varela, D. Depetris, F. de Carlos, J. Cobo, V. Andrés, A. D.
758 Sandre-Giovannoli, J. M. P. Freije, N. Lévy, C. López-Otín, Splicing-directed therapy in a new
759 mouse model of human accelerated aging. *Science translational medicine*. 3, 106ra107-
760 106ra107 (2011).

761 6. M. Puttaraju, M. Jackson, S. Klein, A. Shilo, C. F. Bennett, L. Gordon, F. Rigo, T. Misteli,
762 Systematic screening identifies therapeutic antisense oligonucleotides for Hutchinson–Gilford
763 progeria syndrome. *Nat Med*. 27, 526–535 (2021).

764 7. P. Scaffidi, T. Misteli, Reversal of the cellular phenotype in the premature aging disease
765 Hutchinson-Gilford progeria syndrome. *Nature Medicine*. 11, 440–445 (2005).

766 8. M. R. Erdos, W. A. Cabral, U. L. Tavarez, K. Cao, J. Gvozdenovic-Jeremic, N. Narisu, P. M.
767 Zerfas, S. Crumley, Y. Boku, G. Hanson, D. V. Mourich, R. Kole, M. A. Eckhaus, L. B. Gordon,
768 F. S. Collins, A targeted antisense therapeutic approach for Hutchinson–Gilford progeria
769 syndrome. *Nat Med*. 27, 536–545 (2021).

770 9. O. Santiago-Fernández, F. G. Osorio, V. Quesada, F. Rodríguez, S. Basso, D. Maeso, L.
771 Rolas, A. Barkaway, S. Nourshargh, A. R. Folgueras, J. M. P. Freije, C. López-Otín,
772 Development of a CRISPR/Cas9-based therapy for Hutchinson–Gilford progeria syndrome. *Nat*
773 *Med*. 25, 423–426 (2019).

774 10. J. Swift, I. L. Ivanovska, A. Buxboim, T. Harada, P. C. D. P. Dingal, J. Pinter, J. D.
775 Pajerowski, K. R. Spinler, J.-W. Shin, M. Tewari, F. Rehfeldt, D. W. Speicher, D. E. Discher,
776 Nuclear Lamin-A Scales with Tissue Stiffness and Enhances Matrix-Directed Differentiation.
777 *Science*. 341, 1240104 (2013).

778 11. B. H. Toyama, J. N. Savas, S. K. Park, M. S. Harris, N. T. Ingolia, J. R. Y. III, M. W. Hetzer,
779 Identification of Long-Lived Proteins Reveals Exceptional Stability of Essential Cellular
780 Structures. *Cell*. 154, 971–982 (2013).

781 12. D. Razafsky, C. Ward, C. Potter, W. Zhu, Y. Xue, V. J. Kefalov, L. G. Fong, S. G. Young, D.
782 Hodzic, Lamin B1 and lamin B2 are long-lived proteins with distinct functions in retinal
783 development. *Mol Biol Cell*. 27, 1928–1937 (2016).

784 13. A. Buchwalter, M. W. Hetzer, Nucleolar expansion and elevated protein translation in
785 premature aging. *Nature Communications*, 1–13 (2017).

786 14. J. Hasper, K. Welle, J. Hryhorenko, S. Ghaemmaghami, A. Buchwalter, *Biorxiv*, in press,
787 doi:10.1101/2022.04.24.488979.

788 15. D. Wang, B. Eraslan, T. Wieland, B. Hallström, T. Hopf, D. P. Zolg, J. Zecha, A. Asplund, L.
789 Li, C. Meng, M. Frejno, T. Schmidt, K. Schnatbaum, M. Wilhelm, F. Ponten, M. Uhlen, J.
790 Gagneur, H. Hahne, B. Kuster, A deep proteome and transcriptome abundance atlas of 29
791 healthy human tissues. *Mol Syst Biol*. 15, e8503 (2019).

792 16. B. Schwanhäusser, D. Busse, N. Li, G. Dittmar, J. Schuchhardt, J. Wolf, W. Chen, M.
793 Selbach, Global quantification of mammalian gene expression control. *Nature*. 473, 337–342
794 (2011).

795 17. J. R. Wiśniewski, M. Y. Hein, J. Cox, M. Mann, A "Proteomic Ruler" for Protein Copy
796 Number and Concentration Estimation without Spike-in Standards*. *Mol Cell Proteomics*. 13,
797 3497–3506 (2014).

798 18. J. Swift, I. L. Ivanovska, A. Buxboim, T. Harada, P. C. D. P. Dingal, J. Pinter, J. D.
799 Pajerowski, K. R. Spinler, J.-W. Shin, M. Tewari, F. Rehfeldt, D. W. Speicher, D. E. Discher,
800 Nuclear Lamin-A Scales with Tissue Stiffness and Enhances Matrix-Directed Differentiation.
801 *Science*. 341, 1240104 (2013).

802 19. P. H. Kim, J. Luu, P. Heizer, Y. Tu, T. A. Weston, N. Chen, C. Lim, R. L. Li, P.-Y. Lin, J. C.
803 Y. Dunn, D. Hodzic, S. G. Young, L. G. Fong, Disrupting the LINC complex in smooth muscle
804 cells reduces aortic disease in a mouse model of Hutchinson-Gilford progeria syndrome. *Sci*
805 *Transl Med*. 10, eaat7163 (2018).

806 20. R. Varga, M. Eriksson, M. R. Erdos, M. Olive, I. Harten, F. Kolodgie, B. C. Capell, J. Cheng,
807 D. Faddah, S. Perkins, H. Avallone, H. San, X. Qu, S. Ganesh, L. B. Gordon, R. Virmani, T. N.
808 Wight, E. G. Nabel, F. S. Collins, Progressive vascular smooth muscle cell defects in a mouse
809 model of Hutchinson-Gilford progeria syndrome. *Proceedings of the National Academy of*
810 *Sciences*. 103, 3250–3255 (2006).

811 21. M. R. Hamczyk, R. V. Bellosta, P. Gonzalo, M. J. A. Manzano, P. Nogales, J. F. Bentzon, C.
812 López-Otín, V. Andrés, Vascular Smooth Muscle–Specific Progerin Expression Accelerates
813 Atherosclerosis and Death in a Mouse Model of Hutchinson-Gilford Progeria Syndrome.
814 *Circulation*. 138, 266–282 (2018).

815 22. C. J. Reddel, A. S. Weiss, Lamin A expression levels are unperturbed at the normal and
816 mutant alleles but display partial splice site selection in Hutchinson-Gilford progeria syndrome. *J*
817 *Med Genet*. 41, 715 (2004).

818 23. M. A. D'Angelo, M. Raices, S. H. Panowski, M. W. Hetzer, Age-Dependent Deterioration of
819 Nuclear Pore Complexes Causes a Loss of Nuclear Integrity in Postmitotic Cells. *Cell*. 136,
820 284–295 (2009).

821 24. D. B. McClatchy, M.-Q. Dong, C. C. Wu, J. D. Venable, J. R. Yates, 15N Metabolic Labeling
822 of Mammalian Tissue with Slow Protein Turnover. *J Proteome Res*. 6, 2005–2010 (2007).

823 25. P. Scaffidi, T. Misteli, Lamin A-dependent misregulation of adult stem cells associated with
824 accelerated ageing. *Nature Cell Biology*. 10, 452–459 (2008).

825 26. M. A. Merideth, L. B. Gordon, S. Clauss, V. Sachdev, A. C. M. Smith, M. B. Perry, C. C.
826 Brewer, C. Zalewski, H. J. Kim, B. Solomon, B. P. Brooks, L. H. Gerber, M. L. Turner, D. L.

827 Domingo, T. C. Hart, J. Graf, J. C. Reynolds, A. Gropman, J. A. Yanovski, M. Gerhard-Herman,
828 F. S. Collins, E. G. Nabel, R. O. Cannon, W. A. Gahl, W. J. Introne, Phenotype and course of
829 Hutchinson-Gilford progeria syndrome. *The New England journal of medicine*. 358, 592–604
830 (2008).

831 27. D. Gabriel, D. Roedl, L. B. Gordon, K. Djabali, Sulforaphane enhances progerin clearance in
832 Hutchinson-Gilford progeria fibroblasts. *Aging Cell*. 14, 78–91 (2014).

833 28. M. Eriksson, W. T. Brown, L. B. Gordon, M. W. Glynn, J. Singer, L. Scott, M. R. Erdos, C. M.
834 Robbins, T. Y. Moses, P. Berglund, A. Dutra, E. Pak, S. Durkin, A. B. Csoka, M. Boehnke, T. W.
835 Glover, F. S. Collins, Recurrent de novo point mutations in lamin A cause Hutchinson-Gilford
836 progeria syndrome. *Nature*. 423, 293–298 (2003).

837 29. B. Burke, C. L. Stewart, The nuclear lamins: flexibility in function. *Nature Publishing Group*.
838 14, 13–24 (2012).

839 30. A. C. Peterson, J. D. Russell, D. J. Bailey, M. S. Westphall, J. J. Coon, Parallel Reaction
840 Monitoring for High Resolution and High Mass Accuracy Quantitative, Targeted Proteomics*.
841 *Mol Cell Proteomics*. 11, 1475–1488 (2012).

842 31. G. C. McAlister, E. L. Huttlin, W. Haas, L. Ting, M. P. Jedrychowski, J. C. Rogers, K. Kuhn,
843 I. Pike, R. A. Grothe, J. D. Blethrow, S. P. Gygi, Increasing the Multiplexing Capacity of TMTs
844 Using Reporter Ion Isotopologues with Isobaric Masses. *Anal Chem*. 84, 7469–7478 (2012).

845 32. K. Ben-Harush, N. Wiesel, D. Frenkiel-Krispin, D. Moeller, E. Soreq, U. Aebi, H. Herrmann,
846 Y. Gruenbaum, O. Medalia, The Supramolecular Organization of the C. elegans Nuclear Lamin
847 Filament. *J Mol Biol*. 386, 1392–1402 (2009).

848 33. K. T. Sapra, Z. Qin, A. Dubrovsky-Gaupp, U. Aebi, D. J. Müller, M. J. Buehler, O. Medalia,
849 Nonlinear mechanics of lamin filaments and the meshwork topology build an emergent nuclear
850 lamina. *Nat Commun*. 11, 6205 (2020).

851 34. J. Swift, I. L. Ivanovska, A. Buxboim, T. Harada, P. C. D. P. Dingal, J. Pinter, J. D.
852 Pajerowski, K. R. Spinler, J.-W. Shin, M. Tewari, F. Rehfeldt, D. W. Speicher, D. E. Discher,
853 Nuclear Lamin-A Scales with Tissue Stiffness and Enhances Matrix-Directed Differentiation.
854 *Science*. 341, 1240104 (2013).

855 35. B. Nmezi, J. Xu, R. Fu, T. J. Armiger, G. Rodriguez-Bey, J. S. Powell, H. Ma, M. Sullivan, Y.
856 Tu, N. Y. Chen, S. G. Young, D. B. Stolz, K. N. Dahl, Y. Liu, Q. S. Padiath, Concentric
857 organization of A- and B-type lamins predicts their distinct roles in the spatial organization and
858 stability of the nuclear lamina. *Proc National Acad Sci*. 116, 201810070 (2019).

859 36. J. Hasper, K. Welle, J. Hryhorenko, S. Ghaemmaghami, A. Buchwalter, *Biorxiv*, in press,
860 doi:10.1101/2022.04.24.488979.

861 37. J. A. M. Bard, C. Bashore, K. C. Dong, A. Martin, The 26S Proteasome Utilizes a Kinetic
862 Gateway to Prioritize Substrate Degradation. *Cell*. 177, 286-298.e15 (2019).

863 38. N. F. Bence, R. M. Sampat, R. R. Kopito, Impairment of the Ubiquitin-Proteasome System
864 by Protein Aggregation. *Science*. 292, 1552–1555 (2001).

865 39. B. J. Hindson, K. D. Ness, D. A. Masquelier, P. Belgrader, N. J. Heredia, A. J. Makarewicz,
866 I. J. Bright, M. Y. Lucero, A. L. Hiddessen, T. C. Legler, T. K. Kitano, M. R. Hodel, J. F.
867 Petersen, P. W. Wyatt, E. R. Steenblock, P. H. Shah, L. J. Bousse, C. B. Troup, J. C. Mellen, D.
868 K. Wittmann, N. G. Erndt, T. H. Cauley, R. T. Koehler, A. P. So, S. Dube, K. A. Rose, L.
869 Montesclaros, S. Wang, D. P. Stumbo, S. P. Hodges, S. Romine, F. P. Milanovich, H. E. White,
870 J. F. Regan, G. A. Karlin-Neumann, C. M. Hindson, S. Saxonov, B. W. Colston, High-
871 Throughput Droplet Digital PCR System for Absolute Quantitation of DNA Copy Number. *Anal*
872 *Chem*. 83, 8604–8610 (2011).

873 40. G. C. McAlister, D. P. Nusinow, M. P. Jedrychowski, M. Wühr, E. L. Huttlin, B. K. Erickson,
874 R. Rad, W. Haas, S. P. Gygi, MultiNotch MS3 Enables Accurate, Sensitive, and Multiplexed
875 Detection of Differential Expression across Cancer Cell Line Proteomes. *Anal Chem*. 86, 7150–
876 7158 (2014).

877 41. K. A. Welle, T. Zhang, J. R. Hryhorenko, S. Shen, J. Qu, S. Ghaemmaghami, Time-resolved
878 Analysis of Proteome Dynamics by Tandem Mass Tags and Stable Isotope Labeling in Cell
879 Culture (TMT-SILAC) Hyperplexing*. *Mol Cell Proteomics*. 15, 3551–3563 (2016).

880 42. E. P. Quinlivan, J. F. G. III, DNA digestion to deoxyribonucleoside: A simplified one-step
881 procedure. *Analytical Biochemistry*. 373, 383–385 (2008).

882 43. D. Su, C. T. Y. Chan, C. Gu, K. S. Lim, Y. H. Chionh, M. E. McBee, B. S. Russell, I. R.
883 Babu, T. J. Begley, P. C. Dedon, Quantitative analysis of ribonucleoside modifications in tRNA
884 by HPLC-coupled mass spectrometry. *Nat Protoc*. 9, 828–841 (2014).

885